

1 High Voltage Mg-Ion Battery Cathode via a Solid Solution Cr–Mn 2 Spinel Oxide

3 Bob Jin Kwon,* Liang Yin, Haesun Park, Prakash Parajuli, Khagesh Kumar, Sanghyeon Kim,
 4 Mengxi Yang, Megan Murphy, Peter Zapol, Chen Liao, Timothy T. Fister, Robert F. Klie, Jordi Cabana,
 5 John T. Vaughey, Saul H. Lapidus, and Baris Key*



Cite This: <https://dx.doi.org/10.1021/acs.chemmater.0c01988>



Read Online

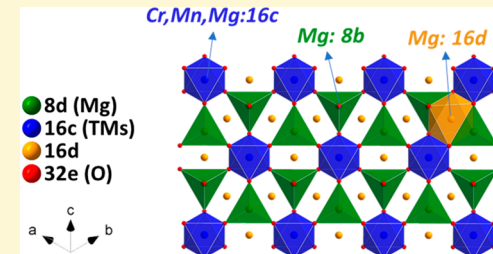
ACCESS |

Metrics & More

Article Recommendations

Supporting Information

6 **ABSTRACT:** Lattice Mg^{2+} in a tailored solid solution spinel, $MgCrMnO_4$, is
 7 electrochemically utilized at high Mn-redox potentials in a nonaqueous electrolyte.
 8 Complementary evidence from experimental and theoretical analyses supports
 9 bulk Mg^{2+} (de)intercalation throughout the designed oxide frame where strong
 10 electrostatic interaction between Mg^{2+} and O^{2-} exists. Mg/Mn antisite inversion in
 11 the spinel is lowered to $\sim 10\%$ via postannealing at $350\text{ }^\circ\text{C}$ to further improve Mg^{2+}
 12 mobility. Spinel lattice is preserved upon removal of Mg^{2+} without any phase
 13 transformations, denoting structural stability at the charged state at a high potential
 14 $\sim 3.0\text{ V}$ (vs Mg/Mg^{2+}). Clear remagnesiation upon first discharge, harvesting up to
 15 $\sim 180\text{ Wh/kg}$ at $60\text{ }^\circ\text{C}$ is shown. In the remagnesiated state, insertion of Mg^{2+} into
 16 interstitial sites in the spinel is detected, possibly resulting in partial reversibility which needs to be addressed for structural stability.
 17 The observations constitute a first clear path to the development of a practical high voltage Mg-ion cathode using a spinel oxide.



18 ■ INTRODUCTION

19 Nonaqueous Mg-ion batteries have been considered as an
 20 alternative to Li-ion technology with the potential to deliver high
 21 energy density at low cost.^{1,2} This strongly depends on the
 22 discovery of cathode materials with reversible storage capacity
 23 operating at high potentials.^{3,4} However, reversible intercalation
 24 of Mg^{2+} has been achieved in a limited number of frameworks,
 25 mainly composed of soft anions, such as Mo_6X_8 ($X = S, Se$) and
 26 TiS_2 .^{5,6} These phases, while being suitable for reversibility and
 27 stability, with their low operating potentials ($\sim 1\text{ V}$ vs Mg/Mg^{2+})
 28 severely limit the energy density of the electrochemical cells
 29 highlighting the need to explore new compounds where Mg^{2+} is
 30 reversibly intercalated at high redox potentials. In theory, the
 31 potential can be raised by utilizing an oxide framework instead,
 32 while preserving structural flexibility that enables and sustains
 33 percolating pathways for Mg^{2+} migration at all states of charge.⁷
 34 However, such paths of Mg^{2+} show relatively high barriers to
 35 cation hopping in oxide lattices, due to the existence of strong
 36 electrostatic interactions between the localized charges at Mg^{2+}
 37 and O^{2-} .^{7,8} Consequently, sluggish migration of Mg^{2+} has been
 38 assigned as the main cause of the poor electrochemical
 39 properties of oxide cathodes with overpotentials so large as to
 40 open up alternate pathways for electrochemical conversion and/
 41 or amorphization instead, where the oxide is reduced by losing
 42 O^{2-} rather than by intercalating Mg^{2+} .^{9,10} As a result, it is
 43 necessary to design new functional oxides, which utilize facile
 44 Mg^{2+} in the lattice at high redox potentials in a nonaqueous
 45 electrolyte.

Theoretical and experimental evidence has revealed that oxide 46 spinels constitute a possible host favorable for intercalation of 47 multivalent cations owing to their three-dimensional pathways 48 of migration.^{8,11} The spinel structures are expected to provide 49 feasible integration of operational potential, capacity, and cation 50 mobility, as indicated in the theoretical predictions.⁸ Feasibility 51 of Mg^{2+} intercalation into host Mn_2O_4 was demonstrated in an 52 aqueous electrolyte system,¹² experimentally, but the activation 53 energy ($\sim 0.8\text{ eV}$) of Mg^{2+} migration in Mn-spinel strongly limits 54 preferential (de)intercalation of Mg^{2+} when conjugated with a 55 nonaqueous Mg electrolyte.^{8,13} Moreover, inversion between 56 Mg^{2+} and Mn^{2+} , by disproportionation of Mn ions,^{14–16} has 57 been observed in a $MgMn_2O_4$ spinel synthesized at high 58 temperatures which raises a barrier of cation migration in the 59 lattices.^{13,16} As an outcome of theoretical screening on various 60 spinels, $MgCr_2O_4$ satisfies relatively facile mobility with $\sim 0.6\text{ eV}$ 61 of activation energy for a Mg^{2+} hop to an adjacent vacancy site,⁶² which is further estimated by density functional theory (DFT),⁶³ solid-state nuclear magnetic resonance (ss-NMR), and muon-⁶⁴ spin relaxation experiments.^{16,17} However, the high redox 65 potentials for (de)intercalation of Mg^{2+} ($\sim 3.7\text{ V}$ vs Mg/Mg^{2+})⁶⁶ preclude the practicality of $MgCr_2O_4$ as a functional cathode⁶⁷

Received: May 11, 2020

Revised: July 14, 2020

Published: July 14, 2020

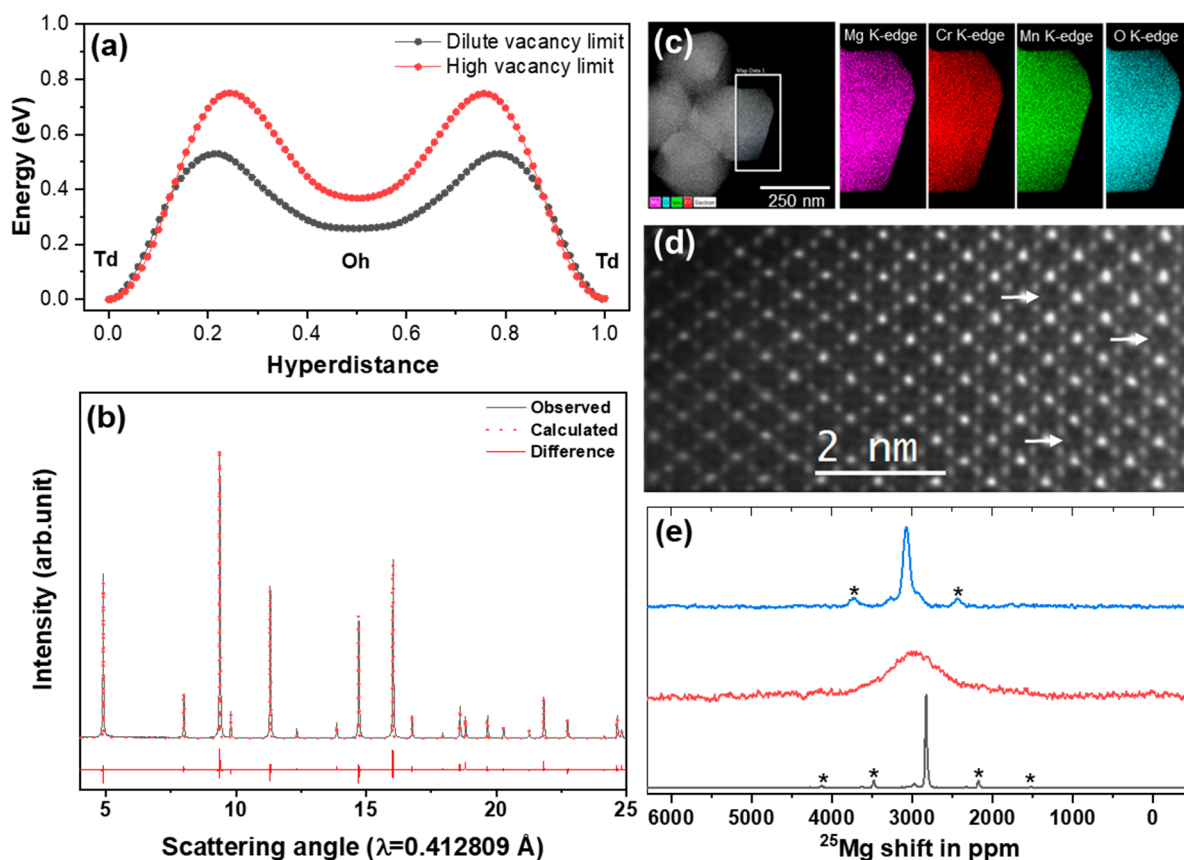


Figure 1. (a) Minimum energy pathways of Mg^{2+} migration in MgCrMnO_4 at the high and dilute vacancy limits. (b) Synchrotron XRD pattern, (c) STEM-EDX mapping, and (d) atomic HAADF image of MgCrMnO_4 along [110] showing spinel structure. Arrows show the nonuniform intensity across the tetrahedral sites within the spinel unit. (e) Solid-state NMR spectra of MgCr_2O_4 (black), MgCrMnO_4 (red), and MgMn_2O_4 (blue). Asterisk marks indicate spinning sidebands.

when paired with current state-of-the-art nonaqueous Mg-ion electrolytes, limiting an upper cutoff potential to ~ 3.5 V (vs Mg/Mg^{2+}).^{8,16} Furthermore, the instability of the oxidized state, $\text{Cr}^{4+}(\text{Ar} 3d^2)$, is another challenge in utilizing Cr redox in spinel lattices, suggesting a necessity for modifying the chemistry.¹⁶

The intrinsic design weaknesses in a single B site Cr- or Mn-spinel for a Mg-ion cathode are alleviated by building a solid-solution MgCrMnO_4 where the mixed transition metal lattice provides mobility via Mg^{2+} bound by Cr^{3+} and suitable high redox potential via Mg^{2+} bound by Mn^{3+} for (de)intercalation. Our recent study on electrochemical Mg^{2+} activity in a largely MgCrVO_4 spinel indicates the feasibility of the design, whereas it also shows partial reversibility of intercalation due to the structural instability and surface reconstruction by removal of Mg^{2+} .¹⁸ In this work, a bulk Mg^{2+} activity with notable reversibility is clearly demonstrated by using a tailored single cubic phase of MgCrMnO_4 spinel in the electrochemical cells, conjugated with a thermally and anodically stable Mg electrolyte.¹⁹ The mechanisms of the (de)intercalation reaction were supported by the combination of experimental and theoretical evidence with consistency. The structures as a response to Mg^{2+} (de)intercalation were examined by X-ray diffraction, microscopic, and spectroscopic characterization experiments at key states of charge. Significant structural and electronic evolutions as a response to Mg^{2+} reactions were observed in the bulk characterization techniques. It is worth noting that the clear

reversible (de)intercalation of Mg^{2+} in spinel oxides has not been achieved so far in nonaqueous electrolytes. These observations of clear bulk Mg^{2+} activity in a Mg-ion cell constitute a fundamental step forward for an oxide spinel to reversibly intercalate Mg^{2+} in a nonaqueous Mg electrolyte through solid-state chemistry design, deepening our understanding on the chemistry of multivalent intercalation and reach a critical milestone in the long quest toward a high energy multivalent ion battery.

RESULTS AND DISCUSSION

The migration barrier of Mg^{2+} in the MgCrMnO_4 lattice was predicted by first-principles calculations at the DFT+U level of theory in both dilute and high vacancy limits (Figure 1a). The Mg^{2+} in the spinel lattices ($T_{\text{d}}-\text{O}_\text{h}-T_{\text{d}}$) migrates through the triangle face shared between the stable and intermediate sites, showing a hill-shaped energy profile.^{16,17} The activation energy of migration reflects a feasible reactivity of Mg^{2+} at the initial and final states upon demagnesiation, utilized by (de)intercalation. The estimated barriers for a Mg^{2+} hop in the Cr-Mn spinel frame were 0.53 eV for dilute vacancy and 0.75 eV for high vacancy limits, similar to the MgCr_2O_4 single B-site spinel, currently known as a framework to provide the most facile Mg^{2+} among oxide spinels (Figure S1 of the Supporting Information, SI). This implies that the degree of Mg^{2+} mobility is not impeded by the introduction of Mn into a spinel in the form of solid-solution, supporting our assumption in designing a functional

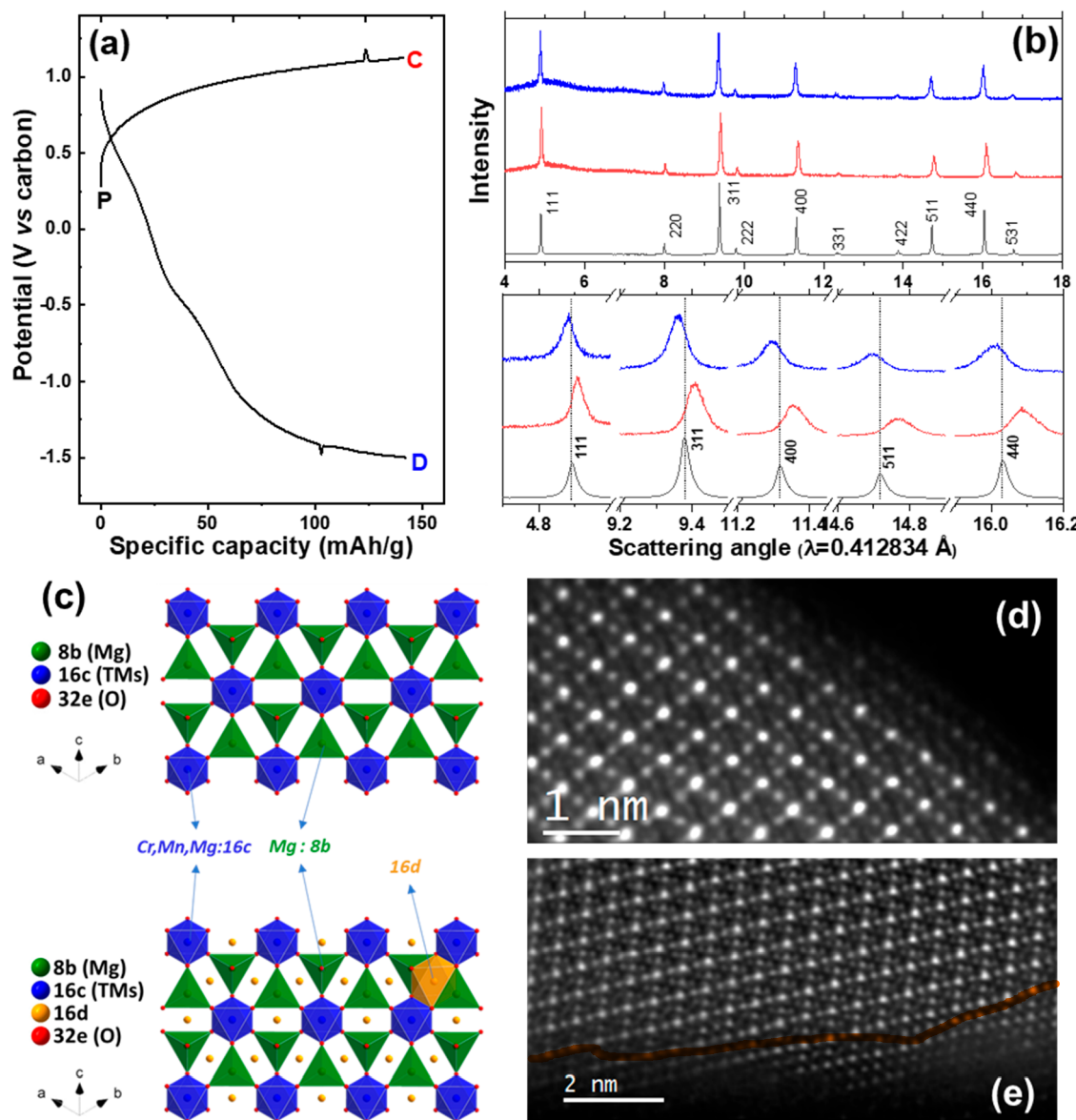


Figure 2. (a) Representative potential versus capacity profile of MgCrMnO_4 measured in a coin cell at 95 °C paired with a carbon counter electrode in $\text{Mg}(\text{TPFA})_2$ electrolyte. (b) Synchrotron XRD patterns of the corresponding pristine (black), charged (red), and discharged (blue) electrode powders in wide and zoom-in angles. (c) Schematic description of two distinct Mg^{2+} occupancies in the remagnesiated spinel (TMs at 16c site indicate Cr or Mn or Mg in the spinel). HAADF-STEM images of (d) charged and (e) discharged MgCrMnO_4 . Charged particle shows the spinel structure across the surface and bulk, whereas rock-salt phase is detected at the surface of the discharged particle.

cathode. The target compound, nanocrystalline MgCrMnO_4 , was synthesized via an aqueous sol–gel route followed by annealing at a controlled temperature (700 °C) to facilitate transition metal mixing while preserving nanoscale particles. The diffraction of pristine MgCrMnO_4 (Figure 1b) indicated a cubic spinel with a parameter of 8.3714(6) Å while presenting no discernible secondary phases or unreacted byproducts. It is worth noting that a cubic symmetry of the spinel with a long-range of order with the existence of Jahn–Teller active Mn^{3+} , could be explained by the high preference of octahedral Cr^{3+} occupancy, possibly suppressing a tetragonal distortion in the assorted lattices. Inversion of Mg/Mn was observed in the Rietveld refinement analysis, with a degree of inversion ($\lambda \approx 0.16$) being attained while presumably, the disproportionation of Mn^{3+} took place simultaneously ($2\text{Mn}^{3+}[\text{O}_h] \rightarrow \text{Mn}^{2+}[\text{T}_d] + \text{Mn}^{4+}[\text{O}_h]$). This thermodynamically favorable cation-

mixing originates from an increase of configurational entropy during high-temperature annealing.¹⁴ For 0.16 inversion, the structural configuration of the spinel could be expressed by $(\text{Mg}_{0.84}\text{Mn}^{2+}_{0.16})^{\text{Td}}[\text{Mg}_{0.16}\text{Cr}^{3+}_{1.00}\text{Mn}^{3+}_{0.68}\text{Mn}^{4+}_{0.16}]^{\text{Oh}}\text{O}_4$. The inversion not only raises the activation barrier of Mg^{2+} in the lattice but also reduces the number of available redox-active Mn^{3+} at octahedral sites, resulting in a reduction of electrochemically utilizable lattice Mg^{2+} .¹⁶ In MgCrMnO_4 , preferential occupancy of octahedral Cr^{3+} with a d^3 electronic configuration^{21,22} mitigates the ratio of antisite disorder in comparison to tetragonal MgMn_2O_4 , a single B-site Mn spinel with $\lambda \approx 0.4$,²³ corresponding to an increase of Mg^{2+} percolation pathways upon electrochemical reactions.¹⁶

The elemental distribution and concentration of pristine MgCrMnO_4 were characterized by STEM-EDX mapping (Figure 1c). We found that magnesium, chromium, and

153 manganese are homogeneously distributed with a stoichiometric
 154 ratio throughout the nanocrystalline particles, consistent with a
 155 solid solution lattice (Figure S2). The average particle size was
 156 measured to be ~ 50 nm using numerous particles imaged in
 157 TEM (Figure S3) which is also similar to the value of ~ 55 nm
 158 estimated from Rietveld refinement. Atomic-resolution images
 159 of MgCrMnO_4 were acquired using high-angle annular dark-
 160 field imaging in an aberration-corrected scanning transmission
 161 electron microscopy (STEM) (Figure 1d). The crystalline spinel
 162 lattice was observed in both the bulk and surface regions of the
 163 particles without any secondary phases or surface layers (Figures
 164 1d and S4). The difference in image contrast at two tetrahedral
 165 sites along the [110] direction was found as indicated by the
 166 arrows in Figure 1d, which is attributed to the presence of Mg/
 167 Mn inversion, consistent with diffraction analysis. The nature of
 168 the Mg^{2+} local environments in the spinel lattice was studied by
 169 solid-state Mg NMR (Figure 1e). The spectra provide Fermi
 170 contact shifts of Mg^{2+} depending on the ensemble of first and
 171 second coordination shells $\text{Mg}-\text{O}-\text{Cr/Mn}$ connectivity in the
 172 lattice due to the presence of paramagnetic centers at Cr^{3+} and
 173 Mn^{3+} (also $\text{Mn}^{2+/4+}$) generating unique spectroscopic signatures
 174 for lattice Mg^{2+} environments alone.^{18,24} The spectra of pristine
 175 MgCrMnO_4 showed a single broad feature with a center of mass
 176 at ~ 2945 ppm (Figure 1e).^{16,24} Appearing exactly halfway
 177 between the sharp resonances due to Mg^{2+} in MgCr_2O_4 (~ 2820
 178 ppm) and MgMn_2O_4 (~ 3070 ppm),²⁴ the broad Gaussian single
 179 peak consistent with random (solid-solution) distribution of
 180 Mg/Cr–Mn in the lattice.¹⁸ Other compositions with higher
 181 and lower Cr:Mn ratios have been successfully synthesized and
 182 will be the focus of future fundamental and applied studies,
 183 respectively. Moreover, no other distinct paramagnetic reso-
 184 nances from contacts between Mg^{2+} and single Cr^{3+} or Mn^{3+} was
 185 detected, indicating no presence of locally segregated clusters.
 186 While the presence of $\text{Mn}^{2+/4+}$ contributes to additional
 187 Gaussian broadening, it does not change the solid-solution
 188 assignment. The peak profile was consistent with ss-NMR²⁵
 189 studies of oxides with random distribution of transition metal in
 190 layered lattices such as $\text{Li}[\text{Ni}_x\text{Mn}_x\text{Co}_{(1-2x)}]\text{O}_2$ ($x = 1/3$) or in
 191 MgMnO_2 rock-salt lattices with random Mg and Mn order-
 192 ing.^{25,26}

193 The electrochemical properties were measured at 95 °C in a
 194 Mg half-cell consisting of an activated carbon counter electrode
 195 and spinel MgCrMnO_4 working electrode with a $\text{Mg}(\text{TPFA})_2$
 196 electrolyte dissolved in triglyme which has shown sufficient
 197 thermal and anodic stability¹⁹ for high-temperature electro-
 198 chemistry (Figure 2a). The primary function of the high surface
 199 area hard carbon is to give rise to sufficient double layer of
 200 charges to match the charge needed to cycle the cathode short-
 201 term, the capacity being completely capacitative.²⁷ The cell was
 202 galvanostatically charged up to the potential at a rate of C/50
 203 where half of the theoretical capacity (~ 140 mAh/g) was
 204 delivered. Then, it was discharged to -1.5 V at a constant
 205 current (C/50) until the same amount of charges was achieved.
 206 The cutoff potential corresponded to only utilization of redox
 207 $\text{Mn}^{3+/4+}$ from a theoretical standpoint, owing to the high
 208 potential of oxidation at $\text{Cr}^{3+/4+}$ in the spinel.^{16,17} The
 209 conditions for the measurement aimed at investigation of
 210 behaviors of Mg^{2+} intercalation when the same amount of
 211 charges were electrochemically de- and reinserted in the oxide.
 212 The anodic reaction proceeded from ~ 0.7 V (vs carbon) and a
 213 specific capacity of ~ 140 mAh/g was reached up to ~ 1.1 V, the
 214 reaction being centered at ~ 1.0 V of a relatively constant
 215 potential (vs carbon). The Mg^{2+} content change upon

216 demagnesiation was measured by SEM-EDX over different
 217 large areas of the electrode (Figure S5), showing a range of
 218 0.24–0.36 mol of deintercalated Mg^{2+} (vs mol of Cr + Mn),
 219 different from 0.5 mol of Mg^{2+} equivalents reacting per mole of
 220 host based on a theoretical formula of MgCrMnO_4 . The
 221 mismatch could be explained by the presence of antisite disorder
 222 by Mg/Mn inversion, which reduces redox-active Mn^{3+} at
 223 octahedral sites to 0.68 mol, which corresponds to 0.34 mol of
 224 utilizable Mg^{2+} and ~ 95 mAh/g of actual capacity stored. Upon
 225 subsequent discharging, the profile was overall sloping with a
 226 discharge capacity of ~ 140 mAh/g, achieved at -1.5 V (vs
 227 carbon), showing dominant overpotentials (Figure 2a).
 228

Synchrotron X-ray diffraction was measured from the same
 229 harvested electrodes to gain insight into the structural evolution
 230 as a response to electrochemical Mg^{2+} reactions (Figure 2b).
 231 Diffraction of the charged electrode showed a distinct shift of
 232 peaks to higher angles in all planes of the cubic lattice as
 233 compared to the pristine, indicating a decrease of the unit cell
 234 volume in the spinel (Table 1). The lattice parameter of the
 235

Table 1. Lattice Parameters and Cell Volumes of Pristine, Charged and Discharged Cubic Spinel MgCrMnO_4 Estimated by the Refinement of XRD Patterns in Figure 2b

state of charge	<i>a</i> parameter (Å)	cell volume (Å ³)
pristine	8.3714(6)	586.68(3)
charged	8.3482(2)	581.82(4)
discharged	8.3928(2)	591.18(5)

236 pristine cubic spinel, 8.3714(6) Å, was significantly contracted
 237 to 8.3482(2) Å in the demagnesiated oxide, while no formation
 238 of secondary phase(s) via conversion reactions were detected. A
 239 visible decrease in the ratio of intensities between (111) and
 240 (311) reflections was observed, correlating to the decrease in
 241 occupancy of tetrahedral Mg^{2+} , distorting the cubic spinel
 242 (Figure S6) consistent with demagnesiation in spinels.¹⁶ To
 243 estimate the maximal level of deintercalation from the pristine
 244 lattice, the spinel was charged up to ~ 1.2 V (vs carbon)
 245 corresponding to ~ 255 mAh/g (Figure S7). No further decrease
 246 in lattice parameter was observed in diffraction, revealing the
 247 apparent amount of electrochemically utilizable Mg^{2+} in the
 248 range of 0.25 to 0.35 mol (elemental composition from SEM-
 249 EDX) consistent with 0.34 mol of the theoretical value. This is
 250 also consistent with the initial assumption that Mn is a main/
 251 sole redox-participating center within the applied potential
 252 window. For the lattice charged up to 1.1 V, upon discharge with
 253 ~ 140 mAh/g of capacity, diffraction peaks were reverted to
 254 lower angles consistent with remagnesiation and reversible
 255 intercalation behavior. Interestingly the peak positions move
 256 further past the pristine, due to an additional increase of lattice
 257 volume (Figure 2b). The lattice parameter of the discharged
 258 oxide was 8.3928(2) Å (Table 1), being larger than the pristine,
 259 suggesting overmagnesiation which was studied in further detail
 260 below. The broad features of peaks in the nanocrystalline oxide
 261 synthesized at 700 °C (~ 50 nm, Figure S3) limited an accurate
 262 refinement of diffraction data for occupancy of reintercalated
 263 Mg^{2+} in the lattice. Consequently, larger particles (~ 270 nm,
 264 Figure S8) with crystallographic long-range ordering for
 265 comparison were synthesized at a higher 950 °C which provides
 266 more suitable diffraction data and in turn crystallographic
 267 information (Figure S9). A reliable dissimilarity was a particle
 268 dimension while structural properties, such as phase purity and a
 269 degree of inversion were nearly identical (Figure S9). Larger
 270

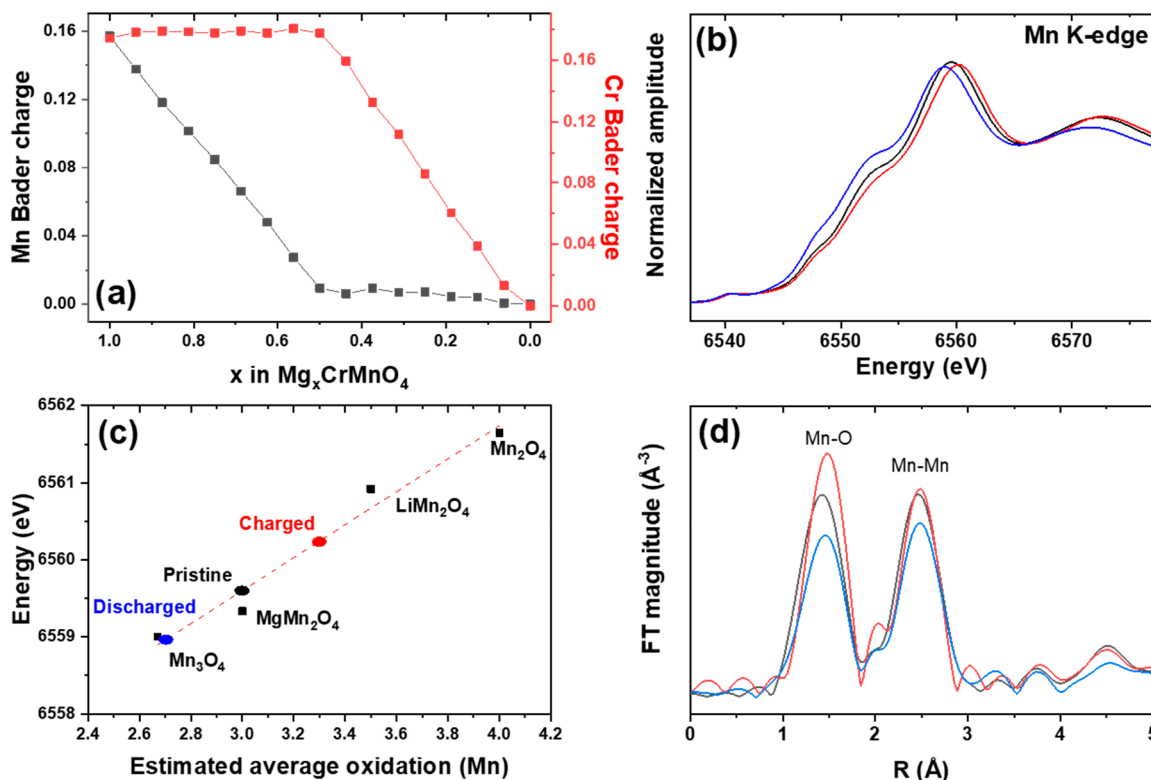


Figure 3. (a) Average Bader charges on Mn (black) and Cr (red) sites in $\text{Mg}_x\text{CrMnO}_4$ structures ($1 \geq x \geq 0$). Bader charges in Mn and Cr spinels are given for comparison. (b) Mn K-edge spectra of pristine (black), charged (red), and discharged (blue) electrodes. (c) The formal valence state of Mn in the samples interpolated from the position of the Mn K-edge onset in the standard spinels. (d) Extended X-ray absorption fine structure of pristine (black), charged (red), and discharged (blue) spinel MgCrMnO_4 .

269 particles induced an increase of overpotentials in the electro-
270 chemical response compared to the nanocrystalline spinel
271 prepared at 700 °C (Figure S9a). A similar degree of the shift to
272 higher angles, with lattice contraction (8.3554 Å) was observed
273 upon demagnesiation. Remagnesiation, interestingly, showed
274 two clearly separate cubic spinel phases with lattice parameters
275 of 8.3811 and 8.4185 Å (Figure S9b). As indicated in the
276 refinement of the remagnesiated state (Figure S10), the
277 reintercalated Mg^{2+} occupied mainly two lattice positions, a
278 main tetrahedral 8b and interstitial octahedral 16d site which
279 correlates closely to the trends observed in the diffraction of the
280 smaller nanocrystals which have significant peak broadening
281 masking these details (Figure 2c).

282 Local structures along the (110) direction at different states of
283 charge were directly visualized by atomic-resolution imaging in
284 STEM (Figure 2d,e). In the demagnesiated nanocrystalline
285 oxide, the spinel lattice was preserved in both the bulk and the
286 surface regions, indicating no structural reformation on the
287 surface by removal of Mg^{2+} , which would be a detrimental
288 phenomenon previously observed.^{18,28,29} Moreover, electron
289 energy-loss spectroscopy (EELS) of the Mn L-edges shows the
290 changes in the Mn valence state as a response to the Mg^{2+}
291 deintercalation while preserving the spinel lattice (Figure
292 S11).³⁰ Upon demagnesiation, the position of the Mn L₃ peak
293 shifts by ~1.2 eV to higher energy indicated oxidation of Mn in
294 the spinel lattices along with a decrease in the ratio of L₃/L₂
295 intensity ($3.37 \rightarrow 2.03$).³¹ Moreover, the multiple empty
296 tetrahedral sites were now visible in the atomic-resolution
297 STEM image in demagnesiated particles (Figure 2d). Therefore,
298 the atomic-resolution characterization confirmed the deinterca-
299 lation of Mg^{2+} from the spinel lattice without phase transition in

300 either the bulk and surface, emphasizing its phase stability at the 300 charged state which is distinct to single B-site spinels.^{16,18,29}
301 However, the discharged oxide showed the presence of rock-salt 302 surface layers with a thickness of ~2 nm (Figure 2e). This 303 observation suggests a transition from spinel to rock-salt on the 304 surface by Mg^{2+} occupying empty octahedral sites in the spinel 305 structure.³² Furthermore, the concentration of Mg^{2+} in the 306 discharged electrode was measured by STEM-EDX elemental 307 mapping (Figure S12). We find an average atomic ratio of $\text{Mg}/$ 308 ($\text{Cr} + \text{Mn}$) in multiple areas of discharged particles of ~0.58 309 (Figure S12), suggesting a comparison of approximately 310 $\text{Mg}_{1.16}\text{CrMnO}_4$. The mechanism of Mg^{2+} intercalation suggests 311 the importance of further optimizing the potential window so as 312 to avoid the formation of rock-salt oxide which presumably can 313 act as a blocking layer and limit reversibility.³¹⁴

315 Changes in average Bader charges on each species of 315 transition metal ions versus Mg^{2+} content in the mixed spinel 316 are shown in Figure 3a. Although a Bader charge typically is 317 f3 much smaller than the formal oxidation state, it is correlated with 318 the latter and provides a reliable measure of oxidation state 319 change.³³ Fully magnesiated, MgCrMnO_4 , showed Cr Bader 320 charge of 1.82e and Mn Bader charge of 1.76e, comparable to 321 1.83e and 1.72e charges in MgCr_2O_4 and MgMn_2O_4 , 322 respectively, and correspond to formal oxidation states of Cr^{3+} 323 and Mn^{3+} . Upon charging, the average charge on Cr ions 324 remains practically the same up to Mg^{2+} content of $x = 0.5$, 325 whereas the average charge on Mn increases linearly with the 326 decrease in Mg^{2+} content and reaches 1.93e, which is the same 327 value as in Mn_2O_4 , and corresponds to the formal oxidation state 328 of Mn^{4+} . Therefore, we conclude that extraction of up to half of 329 Mg^{2+} does not change Cr oxidation state, but results in oxidation 330

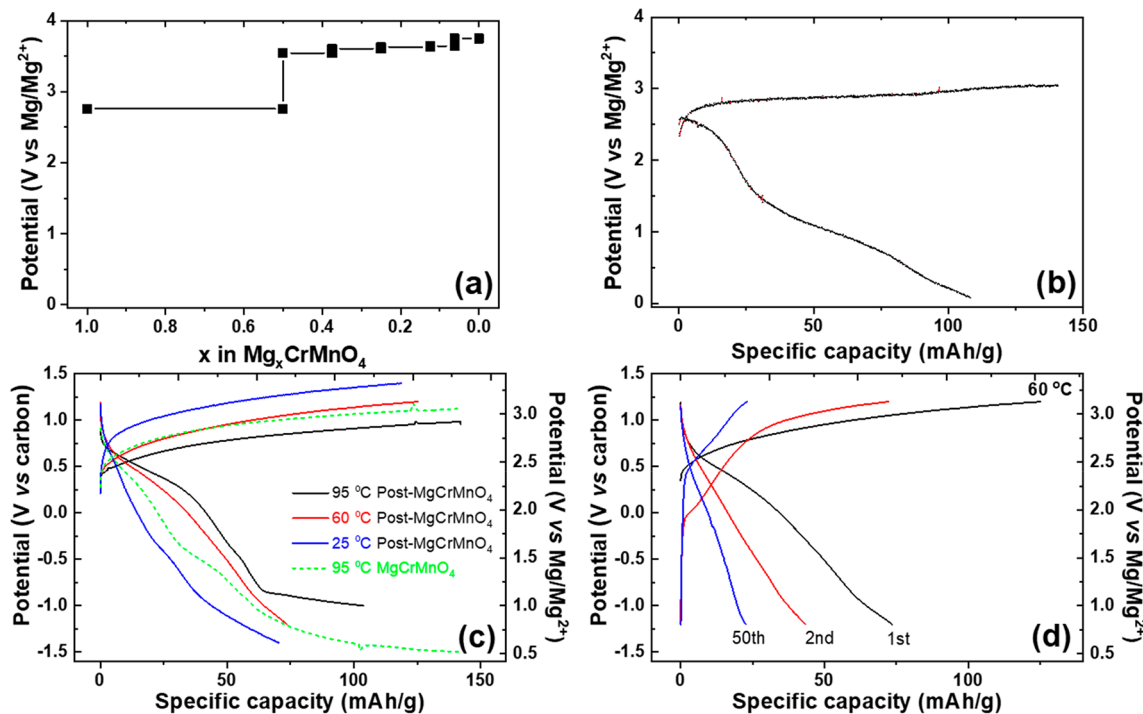


Figure 4. (a) Average potential curves in $\text{Mg}_x\text{CrMnO}_4$ ($1 \geq x \geq 0$), estimated by using the lowest formation energy structures across Mg concentration. (b) Representative potential versus capacity profile of MgCrMnO_4 paired with a Mg foil anode at 95 °C. Representative potential versus capacity profiles of post- MgCrMnO_4 (solid line) and MgCrMnO_4 (dash line) at (c) variable temperatures and (d) the different number of cycles at 60 °C when paired with a carbon counter electrode.

331 of Mn, because of its higher-lying electronic states in the valence
 332 band of the mixed spinel. Continuing extraction of Mg^{2+} beyond
 333 $x = 0.5$ results in a linearly increasing change of average Bader
 334 charge on Cr ions reaching 2.00e at $x = 0$, which is similar to
 335 2.01e charge calculated for a Cr_2O_4 structure¹⁷ with a formal
 336 oxidation state of Cr^{4+} . While the spinel Cr_2O_4 was predicted
 337 previously, the actual formation and/or the stability of Cr^{4+} in
 338 the spinel structure is uncertain due to potential disproportio-
 339 nation into Cr^{3+} and Cr^{6+} . Therefore, we suggest on the basis of
 340 Bader charge analysis, that $\text{Mn}^{3+}/\text{Mn}^{4+}$ redox is dominant in
 341 charge and discharge processes at $x > 0.5$ in this mixed spinel
 342 composition.

343 Mn K-edge X-ray absorption spectroscopy (XAS) was
 344 employed to understand the element-specific evolution of the
 345 electronic environment as a response to the Mg^{2+} reaction
 346 (Figure 3b–d). The absorption edge involves a bound state
 347 electronic transition from an occupied 1s level to empty valence
 348 3p bands of Mn.¹² The energy position of near-edge features is
 349 particularly sensitive to changes in shielding of core electron
 350 binding energy by valence electrons, which tracks the formal
 351 oxidation state of the metals in the bulk. Figure 3b represented
 352 normalized X-ray absorption near edge structure (XANES)
 353 region for pristine, charged, and discharged MgCrMnO_4
 354 electrodes prepared in a half-cell (Figure 2a). Four standards
 355 of Mn-spinel oxides, Mn_3O_4 ($\text{Mn}^{2+}, \text{Mn}^{3+}$), MgMn_2O_4 (Mn^{3+}),
 356 LiMn_2O_4 ($\text{Mn}^{3+}, \text{Mn}^{4+}$), and Mn_2O_4 (Mn^{4+}), were measured to
 357 predict the oxidation state of the ensemble average within each
 358 electrode (Figure S13). The energy threshold, E_0 , of each
 359 spectrum was estimated from points taken at the onset of the
 360 mainline, at $0.2 \leq \mu \leq 0.8$ (Figure 3c). The values of the
 361 standards showed a linear correlation between the energy
 362 threshold and the formal valence state. Following the

363 comparison, the threshold E_0 of the Mn K-edge in the pristine 364 electrode was consistent with the MgMn_2O_4 (Mn^{3+}) standard. 365 The anodic reaction induced a shift of ~ 0.6 eV in the absorption 366 edge toward the lower energy, indicating bulk oxidation of Mn 367 (Figure 3b,c). Upon applying a cathodic current, the absorption 368 edge was shifted back to a position below than the pristine, 369 denoting an over-reduction of Mn, consistent with the X-ray 370 diffraction and microscopic analyses. Distinct levels of over- 371 reduced Mn state between the bulk and surface of the oxide were 372 identified by measuring Mn L-edge spectra collected in a total 373 electron yielding mode, which is sensitive to ~ 5 nm depth of 374 surface information (Figure S14).³⁴ The pristine spectra 375 presented intense absorption features at ~ 639.8 , ~ 641.7 , and 376 ~ 642.9 eV, which can be associated with the expected 377 coexistence of Mn^{2+} , Mn^{3+} , and Mn^{4+} . Comparison with spinel 378 Mn_3O_4 (Figure S14b), it revealed a higher intensity at ~ 641 eV, 379 indicative of a higher ratio of Mn^{3+} in the valences.³⁴ Upon 380 remagnesiation, a dominant Mn^{2+} at ~ 639.9 eV was detected, 381 indicating a formation of rock-salt on the surface which was 382 consistent with microscopic analysis (Figure 2d).³⁴ However, a 383 smaller shift of ~ 0.1 eV to higher energy in the main edge of Cr 384 K-edge spectra was observed upon demagnesiation (Figure 385 S15). Since the electrochemical potential for oxidation was 386 never reached to the predicted potential of $\text{Cr}^{3+}/\text{Cr}^{4+}$,^{16,17} the 387 changes in valence states of Cr could be explained by the 388 delocalized electrons at the oxidized Mn valence in the Cr–Mn 389 mixed lattices or/and the enhanced kinetics of Mg^{2+} coordinated 390 to Cr by the raised cell temperature.¹⁸ The position of the main 391 edge in the oxidized Cr was reverted to the original position 392 upon reintercalation of Mg^{2+} , a reduction of Cr. Reversible 393 changes for metal redox centers supported a bulk Mg^{2+} activity 394 throughout the designed lattice which are consistent with the 395

395 trends observed in the X-ray diffraction and microscopic 396 analyses. Information on local coordination at Mn and Cr in 397 the mixed spinel was extracted by an extended X-ray absorption 398 fine structure (EXAFS) technique (Figure 3d). The magnitude 399 of first coordination corresponding to the average Mn–O 400 bonds, was notably increased, whereas the second coordination 401 due to Mn–Mn bonds showed no significant changes upon 402 demagnesiation (Figure 3d). The changes could be explained by 403 the oxidation of Jahn–Teller active Mn³⁺, which reduced the 404 locally geometric distortion surrounding the Mn ions. 405 Comparison with EXAFS of the Mn standards (Figure S16) 406 also shows a similar trend for the transition from tetragonal 407 MgMn₂O₄ to cubic Mn₂O₄. Reintercalation of Mg²⁺ into the 408 oxidized state induced a decrease of intensities in both 409 coordination shells (Figure 3d). The presence of Mn²⁺, after 410 over-remagnesiation, likely led to the overall increase of local 411 disorder in the spinel lattice. As shown in Figure S17, the 412 changes in Cr coordination were relatively small along with the 413 shift of the main edge, but systematic decreases of magnitudes in 414 both Cr–O and Cr–Cr were observed after the removal of 415 Mg²⁺. The subtle changes could be due to changes in bonding 416 near neighboring Mn sites in the spinel, and/or slightly oxidized 417 Cr valences. In summary, the electronic structures of Cr and Mn 418 were found to systematically support bulk Mg²⁺ activity 419 throughout the lattice.

420 Figure 4a represents the theoretical estimation of average 421 potentials, as a function of Mg²⁺ content in the Cr–Mn spinel 422 oxide calculated using the lowest formation energies at different 423 states of charge (Figure S18).¹⁷ The average potential for the 424 anodic reaction was ~2.8 V (vs Mg/Mg²⁺) at a relatively 425 constant, up to the composition where half of Mg²⁺ was 426 deintercalated by utilizing Mn redox as predicted in Bader 427 charge analysis (Figure 3a). The predicted potentials raise to 428 above ~3.6 V (vs Mg/Mg²⁺) when more than a half of Mg²⁺ 429 deintercalated, upon initializing Cr redox (Figure 4a). The 430 results supported our assumption that Mn is the main redox- 431 participating metal in the Cr–Mn spinel lattice as observed in 432 the spectroscopic analysis. The reaction potentials of the cell 433 paired with carbon capacitance (a half-cell) were converted to 434 the potentials versus Mg/Mg²⁺ by assembling a full-cell 435 conjugated with a Mg metal anode while other conditions of 436 measurement were identical (Figure S19). Similar shapes of 437 anodic reaction were observed in both electrochemical systems, 438 whereas it showed a potential difference of roughly 2.05 V 439 between the cells (Figure S19c,d). This value was used to 440 calibrate the potentials of a half-cell throughout this manuscript. 441 The nanocrystalline MgCrMnO₄ was tested in a full-cell, paired 442 with a Mg foil anode at 95 °C at a rate of C/50 (Figure 4b). The 443 anodic potential for demagnesiation showed a plateau at ~2.9 V 444 (vs Mg/Mg²⁺), similar to the estimation from DFT calculation. 445 Upon the cathodic reaction, overpotentials comparable to the 446 curves of a half-cell at 95 °C, were observed while two inflection 447 points of potentials were presented at ~2.4 V and ~1.5 V (vs 448 Mg/Mg²⁺). The polarization could be explained by the 449 multifaceted issues including sluggish Mg²⁺, poor desolvation 450 of Mg²⁺ at the interfaces, and formation of blocking layers on the 451 electrodes.^{16,18,26}

452 One possible strategy to enhance sluggish Mg²⁺ mobility in 453 this system is the reduction of Mg/Mn antisite disorder, which is 454 shown to affect Mg²⁺ ionic mobility in spinel.¹⁶ An attempt to 455 reduce the ratio of inversion in Mg/Mn sites was made by 456 postannealing the pristine powder at 350 °C (post- 457 MgCrMnO₄), where an exothermic reaction takes place,

458 captured by thermal gravimetric analysis (Figure S20).^{14,16} As 459 shown in Figure S21, the refinement of post-MgCrMnO₄ 459 indicated a decreased ratio of inversion ($\lambda \approx 0.1$) without any 460 segregated new phases, in turn recruiting more extractable lattice 461 Mg²⁺ along with lowered activation barriers for cation 462 migration.^{13,16} The post-MgCrMnO₄ cell at 25 °C presented 463 an enhancement of capacities in both anodic and cathodic 464 reactions within the same potential window compared to the 465 pristine (Figure S22a). However, a decrease of Mg²⁺ (de)- 466 intercalation at room temperature was observed upon the 467 subsequent cycle due to possibly a sluggish behavior of Mg²⁺ 468 migration, desolvation barriers in the electrode/electrolyte 469 interfaces and/or a lack of conductive nature of SEI on the 470 electrode which require further focus in the future (Figure S23). 471 At the raised temperature (95 °C) as shown in Figure S22b, the 472 extent of polarization was reduced remarkably while obtaining 473 an extended capacity at the potential of ~0.4 V (vs carbon), 474 which could be converted to ~2.4 V (vs Mg/Mg²⁺). It is 475 intriguing that the enhancement is solely correlated to the 476 reduced degree of antisite disorder since no other structural or 477 morphological parameters are changed after the postannealing.^{13,16} The kinetics of the electrochemical reaction at various 479 temperatures, another factor for lowering migration barriers in 480 bulk and at interfaces, were investigated by operating the post- 481 MgCrMnO₄ electrode half-cells at 25, 60, and 95 °C (Figure 4c). 482 The anodic potentials for demagnesiation were steadily lowered 483 with increasing cell temperatures, which is ascribed to be 484 improved Mg²⁺ kinetics. Upon remagnesiation, the cathodic 485 curves of the cells, especially at 60 and 95 °C, revealed relatively 486 higher potentials for reduction which corresponds to a dramatic 487 increase in harvested energy density from the material. Simply 488 put, modification of structural complexity enhances utilizable 489 lattice Mg²⁺ and energy in the oxide frame. The cell at 60 °C 490 which provides moderate Mg²⁺ activity along with less 491 decomposition of the electrolyte, was cycled within the 492 potentials between -1.2 and 1.2 V (Figure 4d), which could 493 be approximately converted to a 3.2–0.8 V (vs Mg/Mg²⁺). The 494 cell was galvanostatically charged up to 1.2 V (vs carbon) at a 495 rate of C/50 where ~125 mAh/g of capacity was delivered 496 (Figure 4d). On the subsequent discharging, a capacity of ~75 497 mAh/g with an average voltage of ~2.4 V (vs Mg/Mg²⁺) was 498 achieved by -1.2 V (vs carbon) corresponding to ~180 Wh/kg 499 of energy density, which was close to the values (200–250 Wh/ 500 kg) of the current Li-ion battery technology (Figure S24). While 501 the reversible capacity steadily drops in the following cycles, a 502 discharge capacity of 44 mAh/g and 23 mAh/g were delivered at 503 cycle No. 2 and 50, respectively.

504 The electrode after 50 cycles was analyzed by X-ray diffraction 505 to track any formation of secondary phases produced by 506 undesired reaction pathways, such as conversion (Figure S25). 507 No visible secondary phases were detected whereas two distinct 508 spinel structures larger than the pristine were found via Rietveld 509 refinement analysis. The expanded lattices, very similar to the 510 observed values for remagnesiated larger particles, can again be 511 explained by overmagnesiation at 16d sites, and/or increase of 512 inversion in repeated cycles. While the origin of this interesting 513 reversible phenomenon is not clear as of now, but it will be 514 explored in a follow-up detailed structural study. The electro- 515 chemical results consistently agree with both experimental and 516 theoretical analyses, revealing the mechanism of Mg²⁺ (de)- 517 intercalation within the spinel lattice where strong electrostatic 518 interaction exists. Overall outcomes of this study showed 519 promise to approach a functional Mg-ion spinel oxide cathode 520

521 operated at high potentials at moderate temperatures by
522 electrochemical Mg^{2+} intercalation. All in all, the study provides
523 a pathway for design rules to enhance lattice Mg^{2+} activity,
524 suggesting the next direction of exploring the oxide spinels.

525 ■ CONCLUSIONS

526 In this work, the capability of the tailored $MgCrMnO_4$ spinel to
527 (de)intercalate Mg^{2+} electrochemically at high potentials was
528 evaluated by the theoretical and experimental approaches. High
529 Mg^{2+} activity was observed in bulk, with a remarkable degree of
530 lattice breathing and reversibility. Characterization of key
531 electrochemical states through a combination of X-ray
532 absorption spectroscopy, nuclear magnetic resonance spectroscopy,
533 copy, electron microscopy, density functional theory calculation,
534 and X-ray diffraction revealed structural, compositional, and
535 redox changes, consistent with a reaction mechanism through
536 the (de)intercalation of Mg^{2+} . A potential plateau at roughly 3.0
537 V (vs Mg/Mg^{2+}) for oxidation was shown at a raised
538 temperature of electrochemical reaction (95 °C), consistent
539 with the theoretical estimates. Notable level of reversible Mg^{2+}
540 intercalation was observed, albeit with significant overpotential.
541 We show that it could be mitigated dramatically by reducing the
542 ratio of Mg/Mn inversion in the lattice by postannealing the
543 spinel at 350 °C, enhancing the Mg^{2+} mobility in the lattice.
544 Possible cyclability at moderate temperature (60 °C) was
545 observed along with a ~180 Wh/kg of energy density delivered
546 at the first discharge reaction. This study redefines lattice design
547 via chemical and structural composition of functional spinel
548 oxides utilized by Mg^{2+} intercalation at high potentials. Our
549 findings uncover a new subclass of cathode material for
550 rechargeable Mg-ion batteries.

551 ■ METHODS

552 **Synthesis.** $MgCrMnO_4$, $MgMn_2O_4$, and $MgCr_2O_4$ were synthesized
553 by an aqueous sol–gel reaction, followed by annealing at various
554 temperatures. Magnesium acetate tetrahydrate ($Mg(CH_3COO)_2 \cdot 4H_2O$,
555 Product No. M5661 in Sigma-Aldrich), chromium acetate
556 hydroxide ($Cr_3(CH_3COO)_7(OH)_2$, Product No. 318108 in Sigma-
557 Aldrich), manganese acetate dihydrate ($Mn(CH_3COO)_3 \cdot 4H_2O$,
558 Product No. 215880 in Sigma-Aldrich) were used as a precursor, and
559 citric acid ($C_6H_8O_7$, Product No. C0759 in Sigma-Aldrich) was
560 introduced as a capping agent. 12.5 mmol of precursors and 25.0 mmol
561 of citric acid were dissolved in 200 mL of deionized water and it was
562 stirred vigorously for 30 min. The mixture was then heated at 120 °C to
563 evaporate water until the powder was obtained. The powders were
564 calcined in air at the temperatures (700 and 950 °C), depending on the
565 purpose of synthesis. Post- $MgCrMnO_4$ was obtained by postannealing
566 the pristine oxides at 350 °C in air for 24 h. Standard $MgMn_2O_4$ was
567 synthesized by calcining the precursor at 950 °C for 24 h in air then it
568 was postannealed at 400 °C for 72 h, followed by a quench at room
569 temperature.¹⁶ $MgCr_2O_4$ was prepared by calcining the precursor at
570 950 °C for 24 h in air.

571 **Characterizations** Theoretical values of the average cell potentials
572 and Mg migration barrier of $MgCrMnO_4$ were obtained from density
573 functional theory calculations as implemented in Vienna Ab initio
574 Simulation Package (VASP).³⁵ The core–valence electron interactions
575 were treated using the projector-augmented wave (PAW) potentials.³⁶
576 The exchange-correlation functionals were described by the generalized
577 gradient approximation (GGA) method developed by Perdew–
578 Burke–Ernzerhof (PBE).³⁷ A Hubbard U correction was also added
579 to describe the localization of d-electrons of redox-active species, Cr (U
580 = 3.7 eV) and Mn (U = 3.9 eV).³⁸ The average cell potential was
581 calculated from the energy difference between the charged and
582 discharged phases. The Mg migration barriers are calculated by the
583 nudged elastic band method (NEB) method, where a 2 × 2 × 2
584 supercell of the primitive cell was used to avoid fictitious interactions

585 between periodic images of diffusing atoms.³⁹ The distribution of Cr 586 and Mn atoms in the spinel structure was chosen using the Pymatgen 587 code to minimize the electrostatic energy of the cell. The NEB 588 calculations are performed with GGA functional without U correction 588 as suggested in reference.⁸

589 High-resolution synchrotron X-ray diffraction data were collected at 590
11-BM beamline at the Advanced Photon Source (APS), Argonne 591
National Laboratory (ANL) (λ = 0.412794, 0.412834, 0.412818, 592
0.412828, and 0.457841 Å). Samples were loaded in Kapton capillaries 593
and mounted on bases provided by the APS. Structures were refined 594
using the Rietveld method as implemented in the TOPAS software 595
package (Bruker-AXS, version 6) across a *d*-spacing range of 5.0 Å to 0.5 596
Å. Full Width Half Maximum (fwhm) and Integral Breath (IB) based 597
on volume-weighted column heights (LVol) were estimated by the 598
macro function of “LVol FWHM CS G L” in TOPAS.

599 Atomic-resolution annular dark field and bright field imaging, as well 600
as EELS and EDX spectroscopies, were performed on an aberration- 601
corrected JEOL JEM-ARM200CF operated at 200 kV which can 602
achieve a spatial resolution of ~73 pm. The ARM200CF is equipped 603
with a cold-field emission gun, providing an energy resolution of 350 604
meV, as well as an Oxford X-Max 100TLE windowless silicon drift EDX 605
detector. Images were acquired using high-angle annular dark-field 606
(HAADF) imaging, where the resulting image contrast is proportional 607
to Z^2 , low angle annular dark field (LAADF) imaging, which is sensitive 608
to strain contrast and incoherent annular bright-field (ABF) imaging, 609
which is sensitive to light elements.

610 Solid-state ²⁵Mg magic angle spinning (MAS) NMR experiments 611
were performed at 11.7 T (500 MHz) on a Bruker Avance III 612
spectrometer operating at a Larmor frequency of 30.64 MHz using a 3.2 613
mm MAS probe. The spectra were acquired at a spinning speed of 20 614
kHz using 3.2 mm rotors with a rotor synchronized spin-echo 615
experiment ($90^\circ - \tau - 180^\circ - \tau$) where τ is $1/r$. To ensure quantification 616
in normalized intensity plots, single pulse experiments (data not 617
shown) with recycle delays 0.1 to 1 s were used to confirm signal 618
saturation. All ²⁵Mg shifts were referenced to 5 M $MgCl_2$ (aq.) at 0 619
ppm.

620 The electrochemical performance was evaluated on composites 621
containing the $MgCrMnO_4$ as working electrodes. Electrode slurries 622
were prepared by mixing the active material, Timcal C45 carbon, and 623
6 wt % of a binder solution consisting of polyvinylidene difluoride 624
(PVDF, Solvay) in *N*-methylpyrrolidone (NMP, Sigma-Aldrich) to 625
produce a dry electrode with a 6:2:2 ratio. Then, the slurry was cast on a 626
stainless-steel foil, and it was dried under vacuum at 80 °C to evaporate 627
NMP. The loading level of active oxide in the dry electrodes was 628
adapted to around 4–6 mg/cm². Circular pieces with a diameter of 3/8 629
in. were punched and assembled in two-electrode coin cells in a 630
glovebox filled with inert Ar gas where the levels of water and oxygen 631
contents were ≤ 1.0 ppm. Half-cell measurements were conducted in 632
0.1 M $Mg[TPFA]_2$ ($[TPFA]^- = [(Al(OC(CF_3)_3)_4)^-]$) dissolved in 633
triglyme.¹⁹ The counter electrode was activated carbon, which was 634
prepared by mixing activated carbon, Timcal C45 carbon, and PVDF 635
with a ratio of 8:1:1 (wt%). The high specific surface area of the 636
activated carbon gives rise to sufficient double-layer charging to match 637
the charge needed to cycle the cathode.⁴⁰ Full-cells paired with a 638
magnesium foil (purity 99.9%, Sigma-Aldrich) were built using 0.1 M 639
 $Mg[TPFA]_2$ /triglyme electrolyte. Glass microfiber filters (VWR 640
28297–289) were used as separators in the coin cell experiment.⁶⁴¹
Electrochemical measurements were performed on a MACCOR 642
battery cycler at 25, 60, and 95 °C. The potentials in this report are 643
referenced to the activated carbon or Mg/Mg^{2+} couple depending on 644
the cell configuration. The rate, C/n , was defined as the current density 645
required to achieve a theoretical capacity of $MgCrMnO_4$, $C = 280$ 646
mAh/g, in n hours, assuming the reaction of $MgCrMnO_4 \leftrightarrow Mg^{2+} +$ 647
 $CrMnO_4$. Electrodes harvested for further characterization were 648
washed multiple times with acetonitrile to remove electrolyte residues.⁶⁴⁹

650 Thermal gravimetric analysis was carried out with a SDT-Q600 (TA 650
Instruments) in the temperature ranged from 50 to 800 °C at a heating 651
rate of 3 °C/min under synthetic air.

652 Mn K-edge X-ray absorption near-edge structure (XANES) was 653
performed at the MRCAT bending magnet beamline 10 μ_B at the 654

655 Advanced Photon Source, Argonne National Laboratory (ANL). X-ray
656 absorption spectra were collected in a transmission mode through the
657 electrochemically treated ex-situ electrodes. Energy was scanned by a
658 double-crystal Si (111) monochromator that was detuned by 50% and
659 the incident and transmitted intensity was measured by gas ionization
660 chambers. Mn and Cr metal reference foil were measured
661 simultaneously with each sample for energy calibration. Data analysis
662 was completed using the IFEFFIT package. Mn L_{II, III}-edge X-ray
663 absorption spectroscopy (XAS) measurements were carried out
664 beamline 4-ID-C at Advanced Photon Source (APS) at Argonne
665 National Laboratory (ANL, Lemont, IL). To verify the electronic
666 environment on the surface of the oxides, the Mn L-edge spectra were
667 collected in a total electron yield (TEY) mode at room temperature and
668 under ultrahigh vacuum conditions (below 10⁻⁸ Torr). Contributions
669 from visible light were carefully minimized before the acquisition, and
670 all spectra were normalized by the current from freshly evaporated gold
671 on a fine grid positioned upstream of the main chamber. The measured
672 spectra were aligned by the beamline reference and a basic
673 normalization using a linear background. Standard spinel oxides,
674 Mn₃O₄ and LiMn₂O₄ (Sigma-Aldrich), were used as-received from a
675 commercial supplier. The Mn₂O₄ spinel was prepared by electro-
676 chemical delithiation of LiMn₂O₄ (charge to 4.3 V vs Li/Li⁺) in Gen 2
677 electrolyte paired with a Li foil.³⁰

678 ■ ASSOCIATED CONTENT

679 ■ Supporting Information

680 The Supporting Information is available free of charge at
681 <https://pubs.acs.org/doi/10.1021/acs.chemmater.0c01988>.

682 Minimum energy pathways of Mg²⁺ in MgCr₂O₄; EDX
683 spectra of pristine MgCrMnO₄; particle size distribution
684 of MgCrMnO₄ nanocrystals; HAADF images of
685 MgCrMnO₄; SEM-EDX of charged MgCrMnO₄; syn-
686 chrotron XRD patterns of ex-situ electrodes; potential
687 versus capacity profiles of MgCrMnO₄; corresponding
688 XRD patterns, particle size distribution; potential versus
689 capacity profiles of MgCrMnO₄ synthesized at 950 °C;
690 synchrotron XRD patterns of the ex-situ electrodes;
691 schematic description of the proposed mechanism;
692 LAADF images and EELS spectra of pristine and charged
693 MgCrMnO₄; EDX mapping of discharged MgCrMnO₄;
694 Mn K-edge spectra of Mn spinel standards; Mn L-edge
695 spectra of pristine and discharged MgCrMnO₄ electrodes;
696 Cr K-edge spectra; Mn K-edge extended X-ray absorption
697 fine structure of standard Mn spinels; Cr K-edge extended
698 X-ray absorption fine structure of MgCrMnO₄; ground
699 state hull of Mg_xCrMnO₄ system; potential versus
700 capacity profiles of MgCrMnO₄ in a half- and full-cell;
701 thermal gravimetric analysis of pristine MgCrMnO₄;
702 synchrotron XRD Rietveld refinement of post-
703 MgCrMnO₄; potential versus capacity profiles of
704 MgCrMnO₄ and post-MgCrMnO₄ at various temper-
705 atures; potential versus capacity profiles of post-
706 MgCrMnO₄ at first and second cycle; an incremental
707 capacity plot of cathodic reaction in post-MgCrMnO₄
708 electrode; and synchrotron XRD pattern of the electrode
709 after 50 cycles ([PDF](#))

710 ■ AUTHOR INFORMATION

711 Corresponding Authors

712 **Bob Jin Kwon** — Chemical Sciences and Engineering Division and
713 Joint Center for Energy Storage Research, Argonne National
714 Laboratory, Lemont, Illinois 60439, United States;  orcid.org/0000-0001-7395-0814; Email: blkwon@anl.gov

716 **Baris Key** — Chemical Sciences and Engineering Division and Joint 716
717 Center for Energy Storage Research, Argonne National 717
718 Laboratory, Lemont, Illinois 60439, United States;  orcid.org/0000-0002-1987-1629; Email: bkey@anl.gov 719

720 Authors

721 **Liang Yin** — Joint Center for Energy Storage Research and X-ray 721
722 Science Division, Advanced Photon Source, Argonne National 722
723 Laboratory, Lemont, Illinois 60439, United States;  orcid.org/0000-0001-5396-782X 724

725 **Haesun Park** — Joint Center for Energy Storage Research and 725
726 Materials Science Division, Argonne National Laboratory, 726
727 Lemont, Illinois 60439, United States;  orcid.org/0000-0001-6266-8151 728

729 **Prakash Parajuli** — Joint Center for Energy Storage Research, 729
730 Argonne National Laboratory, Lemont, Illinois 60439, United 730
731 States; Department of Physics, University of Illinois at Chicago, 731
732 Chicago, Illinois 60607, United States 732

733 **Khagesh Kumar** — Joint Center for Energy Storage Research, 733
734 Argonne National Laboratory, Lemont, Illinois 60439, United 734
735 States; Department of Chemistry, University of Illinois at Chicago, 735
736 Chicago, Illinois 60607, United States 736

737 **Sanghyeon Kim** — Chemical Sciences and Engineering Division 737
738 and Joint Center for Energy Storage Research, Argonne National 738
739 Laboratory, Lemont, Illinois 60439, United States 739

740 **Mengxi Yang** — Chemical Sciences and Engineering Division and 740
741 Joint Center for Energy Storage Research, Argonne National 741
742 Laboratory, Lemont, Illinois 60439, United States 742

743 **Megan Murphy** — Joint Center for Energy Storage Research, 743
744 Argonne National Laboratory, Lemont, Illinois 60439, United 744
745 States; Department of Chemistry, University of Illinois at Chicago, 745
746 Chicago, Illinois 60607, United States 746

747 **Peter Zapol** — Joint Center for Energy Storage Research and 747
748 Materials Science Division, Argonne National Laboratory, 748
749 Lemont, Illinois 60439, United States;  orcid.org/0000-0003-0570-9169 749

750 **Chen Liao** — Chemical Sciences and Engineering Division and 750
751 Joint Center for Energy Storage Research, Argonne National 751
752 Laboratory, Lemont, Illinois 60439, United States;  orcid.org/0000-0001-5168-6493 753

754 **Timothy T. Fister** — Chemical Sciences and Engineering Division 754
755 and Joint Center for Energy Storage Research, Argonne National 755
756 Laboratory, Lemont, Illinois 60439, United States;  orcid.org/0000-0001-6537-6170 757

758 **Robert F. Klie** — Joint Center for Energy Storage Research, 758
759 Argonne National Laboratory, Lemont, Illinois 60439, United 759
760 States; Department of Physics, University of Illinois at Chicago, 760
761 Chicago, Illinois 60607, United States;  orcid.org/0000-0003-4773-6667 762

763 **Jordi Cabana** — Joint Center for Energy Storage Research, Argonne 763
764 National Laboratory, Lemont, Illinois 60439, United States; 764
765 Department of Chemistry, University of Illinois at Chicago, 765
766 Chicago, Illinois 60607, United States;  orcid.org/0000-0002-2353-5986 767

768 **John T. Vaughan** — Chemical Sciences and Engineering Division 768
769 and Joint Center for Energy Storage Research, Argonne National 769
770 Laboratory, Lemont, Illinois 60439, United States;  orcid.org/0000-0002-2556-6129 771

772 **Saul H. Lapidus** — Joint Center for Energy Storage Research and 772
773 X-ray Science Division, Advanced Photon Source, Argonne 773
774 National Laboratory, Lemont, Illinois 60439, United States 775

776 Complete contact information is available at: 776
<https://pubs.acs.org/doi/10.1021/acs.chemmater.0c01988> 777

778 Author Contributions

779 B.J.K., J.T.V., and B.K. designed this project. B.J.K. synthesized
780 the samples. L.Y. and S.H.L. collected diffraction and performed
781 the structural characterization. B.J.K. and S.K. performed
782 electrochemical experiments. P.P. and R.F.K. collected electron
783 microscopic data. H.P. and P.Z. performed theoretical
784 calculations. K.K., M.M., T.T.F., and J.C. performed X-ray
785 absorption spectroscopy. M.Y. and C.L. synthesized the Mg
786 electrolyte. B.J.K., L.Y., and B.K. wrote the manuscript, following
787 which all authors approved the final version.

788 Notes

789 The authors declare no competing financial interest.

790 ■ ACKNOWLEDGMENTS

791 This work is solely supported by the Joint Center for Energy
792 Storage Research (JCESR) and Energy Innovation Hub funded
793 by the U.S. Department of Energy (DOE), Office of Science,
794 Basic Energy Sciences. This work made use of instruments in the
795 Electron Microscopy Service, specifically JEOL JEM-
796 ARM200CF in the Research Resources Center, University of
797 Illinois at Chicago. Department of Energy (DOE) Office of
798 Science user facility operated for the DOE Office of Science by
799 Argonne National Laboratory under contract no. DE-AC02-
800 06CH11357. Use of the Advanced Photon Source at Argonne
801 National Laboratory was supported by the U.S. Department of
802 Energy, Office of Science, Office of Basic Energy Sciences, under
803 Contract No. DE-AC02-06CH11357.

804 ■ REFERENCES

805 (1) Levi, E.; Gofer, Y.; Aurbach, D. On the Way to Rechargeable Mg
806 Batteries: The Challenge of New Cathode Materials. *Chem. Mater.* 807 **2010**, 22 (3), 860–868.

808 (2) Muldoon, J.; Bucur, C. B.; Gregory, T. Quest for Nonaqueous
809 Multivalent Secondary Batteries: Magnesium and Beyond. *Chem. Rev.* 810 **2014**, 114 (23), 11683–11720.

811 (3) Mao, M. L.; Gao, T.; Hou, S. Y.; Wang, C. S. A critical review of
812 cathodes for rechargeable Mg batteries. *Chem. Soc. Rev.* **2018**, 47 (23),
813 8804–8841.

814 (4) Song, J.; Sahadeo, E.; Noked, M.; Lee, S. B. Mapping the
815 Challenges of Magnesium Battery. *J. Phys. Chem. Lett.* **2016**, 7 (9),
816 1736–1749.

817 (5) Sun, X. Q.; Bonnick, P.; Duffort, V.; Liu, M.; Rong, Z. Q.; Persson,
818 K. A.; Ceder, G.; Nazar, L. F. A high capacity thiospinel cathode for Mg
819 batteries. *Energy Environ. Sci.* **2016**, 9 (7), 2273–2277.

820 (6) Aurbach, D.; Lu, Z.; Schechter, A.; Gofer, Y.; Givari, H.;
821 Turgeman, R.; Cohen, Y.; Moshkovich, M.; Levi, E. Prototype systems
822 for rechargeable magnesium batteries. *Nature* **2000**, 407 (6805), 724–
823 727.

824 (7) Hannah, D. C.; Gautam, G. S.; Canepa, P.; Ceder, G., On the
825 Balance of Intercalation and Conversion Reactions in Battery
826 Cathodes. *Adv. Energy. Mater.* **2018**, 8 (20), 1800379.

827 (8) Liu, M.; Rong, Z. Q.; Malik, R.; Canepa, P.; Jain, A.; Ceder, G.;
828 Persson, K. A. Spinel compounds as multivalent battery cathodes: a
829 systematic evaluation based on ab initio calculations. *Energy Environ.
Sci.* **2015**, 8 (3), 964–974.

831 (9) Sun, X. Q.; Duffort, V.; Mehdi, B. L.; Browning, N. D.; Nazar, L. F.
832 Investigation of the Mechanism of Mg Insertion in Birnessite in
833 Nonaqueous and Aqueous Rechargeable Mg-Ion Batteries. *Chem.
Mater.* **2016**, 28 (2), 534–542.

835 (10) Arthur, T. S.; Zhang, R. G.; Ling, C.; Glans, P. A.; Fan, X. D.;
836 Guo, J. H.; Mizuno, F. Understanding the Electrochemical Mechanism
837 of K-alpha MnO₂ for Magnesium Battery Cathodes. *ACS Appl. Mater.
Interfaces* **2014**, 6 (10), 7004–7008.

839 (11) Rong, Z. Q.; Malik, R.; Canepa, P.; Gautam, G. S.; Liu, M.; Jain,
840 A.; Persson, K.; Ceder, G. Materials Design Rules for Multivalent Ion
Mobility in Intercalation Structures. *Chem. Mater.* **2015**, 27 (17), 841
6016–6021. 842

(12) Kim, C.; Phillips, P. J.; Key, B.; Yi, T. H.; Nordlund, D.; Yu, Y. S.;
843 Bayliss, R. D.; Han, S. D.; He, M. N.; Zhang, Z. C.; Burrell, A. K.; Klie, R.
844 F.; Cabana, J. Direct Observation of Reversible Magnesium Ion
845 Intercalation into a Spinel Oxide Host. *Adv. Mater.* **2015**, 27 (22), 846
3377–3384. 847

(13) Gautam, G. S.; Canepa, P.; Urban, A.; Bo, S. H.; Ceder, G.
848 Influence of Inversion on Mg Mobility and Electrochemistry in Spinels. 849
Chem. Mater. **2017**, 29 (18), 7918–7930. 850

(14) Zhang, X. W.; Zunger, A. Diagrammatic Separation of Different 851
Crystal Structures of $\text{A}(2)\text{BX}(4)$ Compounds Without Energy 852
Minimization: A Pseudopotential Orbital Radii Approach. *Adv. Funct.
Mater.* **2010**, 20 (12), 1944–1952. 853

(15) Radhakrishnan, N. K.; Biswas, A. B. Cation Distribution in 855
Tetragonal Spinel MgMn_2O_4 . *Z. Kristallogr. - Cryst. Mater.* **1975**, 142 856
(1–2), 117–120. 857

(16) Bayliss, R. D.; Key, B.; Sai Gautam, G.; Canepa, P.; Kwon, B. J.;
858 Lapidus, S. H.; Dogan, F.; Adil, A. A.; Lipton, A. S.; Baker, P. J.; et al.
859 Probing Mg Migration in Spinel Oxides. *Chem. Mater.* **2020**, 32 (2), 860
663–670. 861

(17) Chen, T. N.; Gautam, G. S.; Huang, W. X.; Ceder, G. First- 862
Principles Study of the Voltage Profile and Mobility of Mg Intercalation 863
in a Chromium Oxide Spinel. *Chem. Mater.* **2018**, 30 (1), 153–162. 864

(18) Kwon, B. J.; Lau, K.-C.; Park, H.; Wu, Y. A.; Hawthorne, K. L.; Li,
865 H.; Kim, S.; Bolotin, I. L.; Fister, T. T.; Zapol, P.; et al. Probing 866
Electrochemical Mg-Ion Activity in $\text{MgCr}_{2-x}\text{V}_x\text{O}_4$ Spinel Oxides. *Chem.
Mater.* **2020**, 32 (3), 1162–1171. 867

(19) Lau, K. C.; Seguin, T. J.; Carino, E. V.; Hahn, N. T.; Connell, J.
868 G.; Ingram, B. J.; Persson, K. A.; Zavadil, K. R.; Liao, C. Widening 870
Electrochemical Window of Mg Salt by Weakly Coordinating 871
Perfluoroalkoxyaluminate Anion for Mg Battery Electrolyte. *J. Electro-
chem. Soc.* **2019**, 166 (8), A1510–A1519. 872

(20) Golikov, Y. V.; Barkhatov, V. P.; Balakirev, V. F.; Chufarov, G. I.
874 Thermal-Dissociation and Reduction of MgMn_2O_4 . *Zh. Fiz. Khim.* **1982**, 56 (12), 2965–2967. 875

(21) Stefan, E.; Connor, P. A.; Azad, A. K.; Irvine, J. T. S. Structure and 877
properties of $\text{MgM}_x\text{Cr}_{2-x}\text{O}_4$ ($M = \text{Li, Mg, Ti, Fe, Cu, Ga}$) spinels for 878
electrode supports in solid oxide fuel cells. *J. Mater. Chem. A* **2014**, 2 879
(42), 18106–18114. 880

(22) West, A. R. *Solid State Chemistry and its Applications*; John Wiley 881
& Sons, 2014. 882

(23) Radhakrishnan, N. K.; Biswas, A. B. Neutron-Diffraction Study of 883
Cation Migration in MgMn_2O_4 . *Phys. Status Solidi A* **1976**, 37 (2), 719. 884

(24) Lee, J.; Seymour, L. D.; Pell, A. J.; Dutton, S. E.; Grey, C. P. A 885
systematic study of Mg-25 NMR in paramagnetic transition metal 886
oxides: applications to Mg-ion battery materials. *Phys. Chem. Chem.
Phys.* **2017**, 19 (1), 613–625. 887

(25) Zeng, D. L.; Cabana, J.; Breger, J. L.; Yoon, W. S.; Grey, C. P. 889
Cation ordering in $\text{Li}[\text{Ni}_x\text{Mn}_x\text{Co}_{(1-2x)}]\text{O}_2$ -layered cathode materials: A 890
nuclear magnetic resonance (NMR), pair distribution function, X-ray 891
absorption spectroscopy, and electrochemical study. *Chem. Mater.* **2007**, 19 (25), 6277–6289. 893

(26) Wang, H.; Senguttuvan, P.; Proffit, D. L.; Pan, B. F.; Liao, C.;
894 Burrell, A. K.; Vaughey, J. T.; Key, B. Formation of MgO during 895
Chemical Magnesiation of Mg-Ion Battery Materials. *ECS Electrochem.
Lett.* **2015**, 4 (8), A90. 896

(27) Ruch, P. W.; Cericola, D.; Hahn, M.; Kotz, R.; Wokaun, A. On 898
the use of activated carbon as a quasi-reference electrode in non- 899
aqueous electrolyte solutions. *J. Electroanal. Chem.* **2009**, 636 (1–2), 900
128–131. 901

(28) Nam, K. W.; Kim, S.; Lee, S.; Salama, M.; Shterenberg, I.; Gofer,
902 Y.; Kim, J. S.; Yang, E.; Park, C. S.; Kim, J. S.; Lee, S. S.; Chang, W. S.;
903 Doo, S. G.; Jo, Y. N.; Jung, Y.; Aurbach, D.; Choi, J. W. The High 904
Performance of Crystal Water Containing Manganese Birnessite 905
Cathodes for Magnesium Batteries. *Nano Lett.* **2015**, 15 (6), 4071– 906
4079. 907

(29) Truong, Q. D.; Devaraju, M. K.; Tran, P. D.; Gambe, Y.; Nayuki,
908 K.; Sasaki, Y.; Honma, I. Unravelling the Surface Structure of 909

910 MgMn_2O_4 Cathode Materials for Rechargeable Magnesium-Ion
911 Battery. *Chem. Mater.* **2017**, *29* (15), 6245–6251.

912 (30) Kwon, B. J.; Dogan, F.; Jokisaari, J. R.; Key, B.; Kim, C.; Liu, Y. S.;
913 Guo, J. H.; Klie, R. F.; Cabana, J. Effect of Passivating Shells on the
914 Chemistry and Electrode Properties of LiMn_2O_4 Nanocrystal
915 Heterostructures. *ACS Appl. Mater. Interfaces* **2019**, *11* (4), 3823–
916 3833.

917 (31) Kim, C.; Adil, A. A.; Bayliss, R. D.; Kinnibrugh, T. L.; Lapidus, S.
918 H.; Nolis, G. M.; Freeland, J. W.; Phillips, P. J.; Yi, T. H.; Yoo, H. D.;
919 Kwon, B. J.; Yu, Y. S.; Klie, R.; Chupas, P. J.; Chapman, K. W.; Cabana,
920 J. Multivalent Electrochemistry of Spinel $\text{Mg}_x\text{Mn}_{3-x}\text{O}_4$ Nanocrystals.
921 *Chem. Mater.* **2018**, *30* (5), 1496–1504.

922 (32) Shimokawa, K.; Atsumi, T.; Harada, M.; Ward, R. E.; Nakayama,
923 M.; Kumagai, Y.; Oba, F.; Okamoto, N. L.; Kanamura, K.; Ichitsubo, T.
924 Zinc-based spinel cathode materials for magnesium rechargeable
925 batteries: toward the reversible spinel-rocksalt transition. *J. Mater.*
926 *Chem. A* **2019**, *7* (19), 12225–12235.

927 (33) Tang, W.; Sanville, E.; Henkelman, G. E. Henkelman, G. A grid-
928 based Bader analysis algorithm without lattice bias. *J. Phys.: Condens.*
929 *Matter* **2009**, *21* (8), 084204.

930 (34) Nolis, G. M.; Adil, A.; Yoo, H. D.; Hu, L. H.; Bayliss, R. D.;
931 Lapidus, S. H.; Berkland, L.; Phillips, P. J.; Freeland, J. W.; Kim, C.; Klie,
932 R. F.; Cabana, J. Electrochemical Reduction of a Spinel-Type
933 Manganese Oxide Cathode in Aqueous Electrolytes with Ca^{2+} or
934 Zn^{2+} . *J. Phys. Chem. C* **2018**, *122* (8), 4182–4188.

935 (35) Kresse, G.; Furthmüller, J. Efficient iterative schemes for ab initio
936 total-energy calculations using a plane-wave basis set. *Phys. Rev. B: Condens. Matter Mater. Phys.* **1996**, *54* (16), 11169–11186.

937 (36) Blochl, P. E. Projector Augmented-Wave Method. *Phys. Rev. B: Condens. Matter Mater. Phys.* **1994**, *50* (24), 17953–17979.

938 (37) Perdew, J. P.; Burke, K.; Ernzerhof, M. Generalized gradient
939 approximation made simple. *Phys. Rev. Lett.* **1996**, *77* (18), 3865–3868.

940 (38) Dudarev, S. L.; Botton, G. A.; Savrasov, S. Y.; Humphreys, C. J.;
941 Sutton, A. P. Electron-energy-loss spectra and the structural stability of
942 nickel oxide: An LSDA+U study. *Phys. Rev. B: Condens. Matter Mater.*
943 *Phys.* **1998**, *57* (3), 1505–1509.

944 (39) Henkelman, G.; Überuaga, B. P.; Jónsson, H. A climbing image
945 nudged elastic band method for finding saddle points and minimum
946 energy paths. *J. Chem. Phys.* **2000**, *113* (22), 9901–9904.

947 (40) Yoo, H. D.; Jokisaari, J. R.; Yu, Y.-S.; Kwon, B. J.; Hu, L.; Kim, S.;
948 Han, S.-D.; Lopez, M.; Lapidus, S. H.; Nolis, G. M.; et al. Intercalation
949 of Magnesium into a Layered Vanadium Oxide with High Capacity.
950 *ACS Energy Lett.* **2019**, *4* (7), 1528–1534.